Curvilinear features in the southern hemisphere observed by Mars Global Surveyor Mars Orbiter Camera

Huiqun Wang [a,*], Anthony D. Toigo [b,1], Mark I. Richardson [c]

[a] Atomic and Molecular Physics, Harvard-Smithsonian Center for Astrophysics, 60 Garden Street, Cambridge, MA 02138, USA
[b] Center for Radiophysics and Space Research, 326 Space Sciences Building, Cornell University, Ithaca, NY 14853, USA
[c] Ashima Research, Pasadena, CA 91106, USA

ABSTRACT

We have used the complete set of Mars Global Surveyor (MGS) Mars Daily Global Maps (MDGMs) to study martian weather in the southern hemisphere, focusing on curvilinear features, including frontal events and streaks. "Frontal events" refer to visible events that are morphologically analogous to terrestrial baroclinic storms. MDGMs show that visible frontal events were mainly concentrated in the 210–300°E (60–150°W) sector and the 0–60°E sector around the southern polar cap during L_s = 140–250° and L_s = 340–60°. The non-uniform spatial and temporal distributions of activity were also shown by MGS Thermal Emission Spectrometer transient temperature variations near the surface. "Streaks" refer to long curvilinear features in the polar hood or over the polar cap. They are an indicator of the shape of the polar vortex. Streaks in late winter usually show wavy segments between the 180° meridian and Argyre. Model results suggest that the zonal wave number m = 3 eastward traveling waves are important for their formation.

© 2011 Elsevier Inc. All rights reserved.

1. Introduction

Dust storms and clouds are important components of martian weather. Their morphologies, motions and distributions illuminate the underlying circulation. They can also affect the circulation through radiative–dynamic feedbacks (Basu et al., 2006; Kahre et al., 2006; Rafkin, 2009; Wilson et al., 2007, 2008). Mars Global Surveyor (MGS) systematically monitored martian weather with the wide angle Mars Orbiter Camera (MOC) from April 1999 to October 2006. Mars Reconnaissance Orbiter (MRO) Mars Color Imager (MARCI) has continued the daily global imaging of Mars since September 2006; however, data from that instrument is not used in this study. These images have provided detailed information on dust storms and clouds (Cantor et al., 2001, 2010; Cantor, 2007; Wang and Ingersoll, 2002), including global dust storms (Cantor, 2007; Strausberg et al., 2005), frontal/flushing events (Cantor et al., 2010; Hinson and Wang, 2010; Wang et al., 2003, 2005; Wang, 2007) and topographic clouds (Benson et al., 2003; Cantor et al., 2010; Wang and Ingersoll, 2002). The main purpose of this paper is to present MGS MOC observations of the southern hemisphere curvilinear clouds and dust storms, including frontal events and streaks.

We generally refer to curvilinear dust or cloud features which are not apparently related to topography as "frontal events", except when they occur over the polar cap and/or appear as bundles in the polar hood, in which case, we call them "streaks". Clouds and dust storms that exhibit other morphologies are not considered in this paper. The morphologies, configurations and distributions of curvilinear clouds and dust storms suggest the influence of convergence and/or shear in the circulation. Here, we use "frontal events" and "streaks" simply as morphological indicators, independent of the mesoscale dynamical mechanism, which is beyond the scope of this paper.

The complete set of MGS Mars Daily Global Maps (MDGMs) covering the period from L_s = 150° in Mars Year 24 to L_s = 120° in Mars Year 28 (May 1999–October 2006, see Clancy et al. (2000) for the definition of Mars year) has been used for this study. Each MDGM is composed using 13 pairs of red and blue global map swaths taken by MGS MOC around 2 PM local time each day (Wang and Ingersoll, 2002). The nominal resolution of a MGS global map swath is 7 km/pixel (some 3.75 km/pixel), and that of a MDGM is 0.1° longitude × 0.1° latitude (approximately 60 km/pixel near the equator). Dust storms appear yellow/red, while condensate clouds appear blue/white in MDGMs. The MGS Thermal Emission Spectrometer (TES) version 2 temperature data downloaded from the website http://pds-geosciences.wustl.edu have been used to provide supplementary information in this paper. Concurrent TES temperature data exist for the period before August 2004. MarsWRF (Richardson et al., 2007) General Circulation Model

* Corresponding author.
E-mail address: hwang@cfa.harvard.edu (H. Wang).
[1] Present address: Johns Hopkins University, Applied Physics Laboratory, Laurel, MD 20723, USA.

(GCM) simulations have been performed to drive an off-line Lagrangian tracer transport model (Eluszkiewicz et al., 1995; Wang et al., 2003) to examine the effects of various wind components on the formation of wavy streaks over the south polar cap in late winter.

2. Frontal events

Dust or ice aerosols suspended in the atmosphere can be concentrated by winds into curvilinear features. These curvilinear features have been referred to as "frontal events" in studies for the northern hemisphere due to their morphological similarities to terrestrial baroclinic storms in satellite images (Cantor et al., 2010; Wang et al., 2003, 2005; Wang, 2007; Wang and Fisher, 2009). While many "frontal events" may develop in a manner somewhat similar to terrestrial baroclinic storms (near surface convergence and upwelling), the underlying mesoscale dynamics cannot be determined from the images alone. Notwithstanding small-scale dynamical uncertainties, and in keeping with the original analogy, we call all non-topographic arc shaped clouds/dust storms that are not part of the polar hood or exclusively over the polar cap as frontal events. In this paper, we derive statistics for the southern hemisphere frontal events observed in MDGMs and compare them with the relevant results derived from TES thermal observations.

Fig. 1 shows representative southern hemisphere frontal events in the vicinity of the southern polar cap in mid spring (a and b), late summer (c and d) and early fall (e and f). Most observed frontal events lasted for between a few hours and two sols. The configurations of the frontal events in Fig. 1c and d indicate the presence of planetary waves. There appear to be vortices at the southern tips of some arcs in Fig. 1d, analogous to those in occluded fronts. Wang
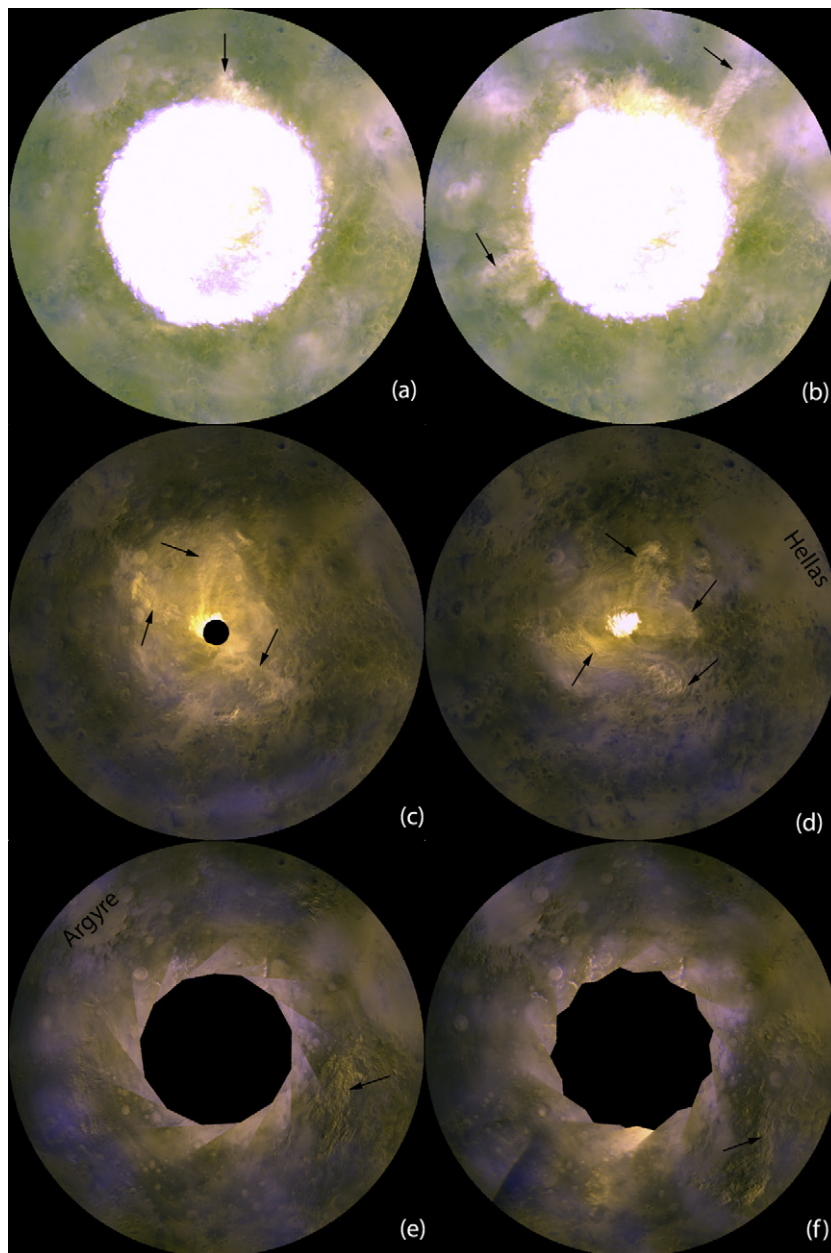
Fig. 1. Frontal events in the south polar Mars Daily Global Maps in polar stereographic projection for the area south of 45°S. The black area at the center of subfigures c, e and f is due to missing data in polar night. Arrows indicate frontal events. (a) $L_s = 222.2°$ in Mars Year 24 (b) $L_s = 227.6°$ in Mars Year 27 (c) $L_s = 354.6°$ in Mars Year 24 (d) $L_s = 346.4°$ in Mars Year 25 (e) $L_s = 22.3°$ in Mars Year 27 (f) $L_s = 28.2°$ in Mars Year 27.

and Ingersoll (2003) showed that cloud tracked winds in the 60–80°S latitudinal band during L$_s$ = 340–10° were generally southeastward (−1 m/s to −10 m/s in the meridional direction, and 5 m/s to 20 m/s in the zonal direction) and occasionally southwestward in the 90–180°E sector. Lee waves in the vicinity of the south polar cap during the fall and winter indicate eastward (westerly) zonal winds (Wang and Ingersoll, 2002) which are consistent (via the thermal wind relation) with the temperature gradients derived from TES data (Smith, 2008). MDGMs showed daily changes in the morphologies, positions and configurations of the frontal events, suggesting that they were associated with transient eddies in the atmosphere. MDGMs showed a few north–south elongated dust plumes in the southern tropical latitudes. There were no clear indications that they were related to any previous frontal events. The southern hemisphere frontal events observed by MGS did not appear to flush dust substantially equatorward, unlike some of their northern hemisphere counterparts (Wang et al., 2003, 2005; Wang, 2007).

We have archived frontal events in the southern hemisphere using MGS MDGMs. The archive includes the solar longitude, the positions of both end points, the length between the end points and the position of a representative point for each frontal event. The representative point is usually in the middle of a curvilinear feature, at the inflection point of a curve, or at the center of a vortex. Vortices (Fig. 1d) were observed in about 1% of the recorded cases. Large scale curvilinear features in the polar hood or over

the polar cap that are indicative of the shape of the polar vortex were classified as "streaks" in this paper (see Section 3 for more discussions).

Significantly fewer visible frontal events were observed in the southern hemisphere than in the northern hemisphere. We recorded a total of 866 frontal events in the southern hemisphere for the whole time period from mid southern winter of Mars Year 24 to early southern winter of Mars Year 28. In comparison, we recorded 2422 frontal events in the northern hemisphere just for the northern springs and summers of the same time period (Wang and Fisher, 2009). This is consistent with Banfield et al.'s (2004) finding from TES temperature data that traveling waves in the southern hemisphere were much weaker than those in the northern hemisphere.

2.1. Seasonal distribution

Fig. 2 shows the seasonal and latitudinal distribution of all the southern hemisphere frontal events in MGS MDGMs (from L$_s$ = 150° in Mars Year 24 to L$_s$ = 120° in Mars Year 28). The 2 PM zonal mean TES surface temperature contours for Mars Year 26 are superimposed on the plot. The nearly four Mars year record of frontal events exhibit a general seasonality: frontal events are concentrated in the vicinity of the seasonal polar cap edge during L$_s$ = 140–250° (mid-winter to late spring) and L$_s$ = 340–60° (late
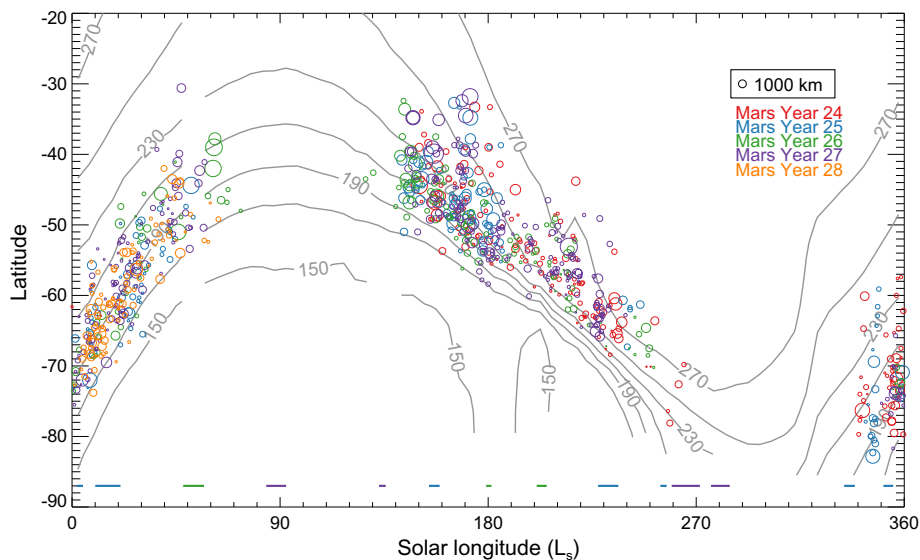

Fig. 2. Solar longitude (L$_s$) versus latitude distribution of southern hemisphere frontal events observed in MGS Mars Daily Global Maps from L$_s$ = 150° in Mars Year 24 to L$_s$ = 120° in Mars Year 28. Each circle is centered on the representative point of the frontal event (see Section 2). The diameter of the circle indicates the length of the frontal event, not the latitudinal extent. The horizontal line segments along 87°S indicate major data gaps of Mars Daily Global Maps. Different colors correspond to different Mars years indicated by the legend. The gray contours are the zonal mean 2PM surface temperatures in Mars Year 26 derived from MGS TES nadir data.
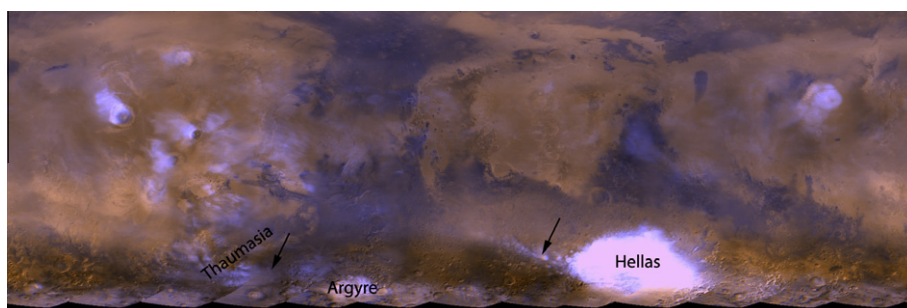
Fig. 3. Mars Daily Global Map in simple cylindrical projection (180°W–180°E, 60°S–60°N) at L$_s$ ~ 104° in Mars Year 26. The black area at the bottom is due to missing data in the polar night. The two linear clouds shown with black arrows, to the west of Hellas and between Thaumasia Fossae and Argyre, occurred almost daily.

summer to mid-fall). There are 462 frontal events during $L_s = 140$–$250°$, and 386 during $L_s = 340$–$60°$. Both periods have some relatively large frontal events whose lengths are greater than 1000 km. Some frontal events near the fall equinox were substantially larger than the polar cap at the time, and their configurations in MDGMs suggested the effects of planetary waves (Fig. 1c and d). In Mars Year 25, frontal events disappeared near $L_s = 185°$ and did not come back until about $L_s = 235°$ (blue circles in Fig. 2), suggesting a possible influence of the 2001 global dust storm.

Southern hemisphere frontal events were rarely observed in the MDGMs during $L_s = 260$–$340°$. This is consistent with TES observations that traveling waves diminished in the lower atmosphere at the southern high latitudes in summer (Banfield et al., 2003, 2004). However, individual global map swaths in southern summer showed occasional curvilinear dust storms near the small south polar cap, especially away from the 2PM side of the image (Wang and Ingersoll, 2002; Toigo et al., 2002). Using mesoscale simulations, Toigo et al. (2002) showed that cap edge dust lifting
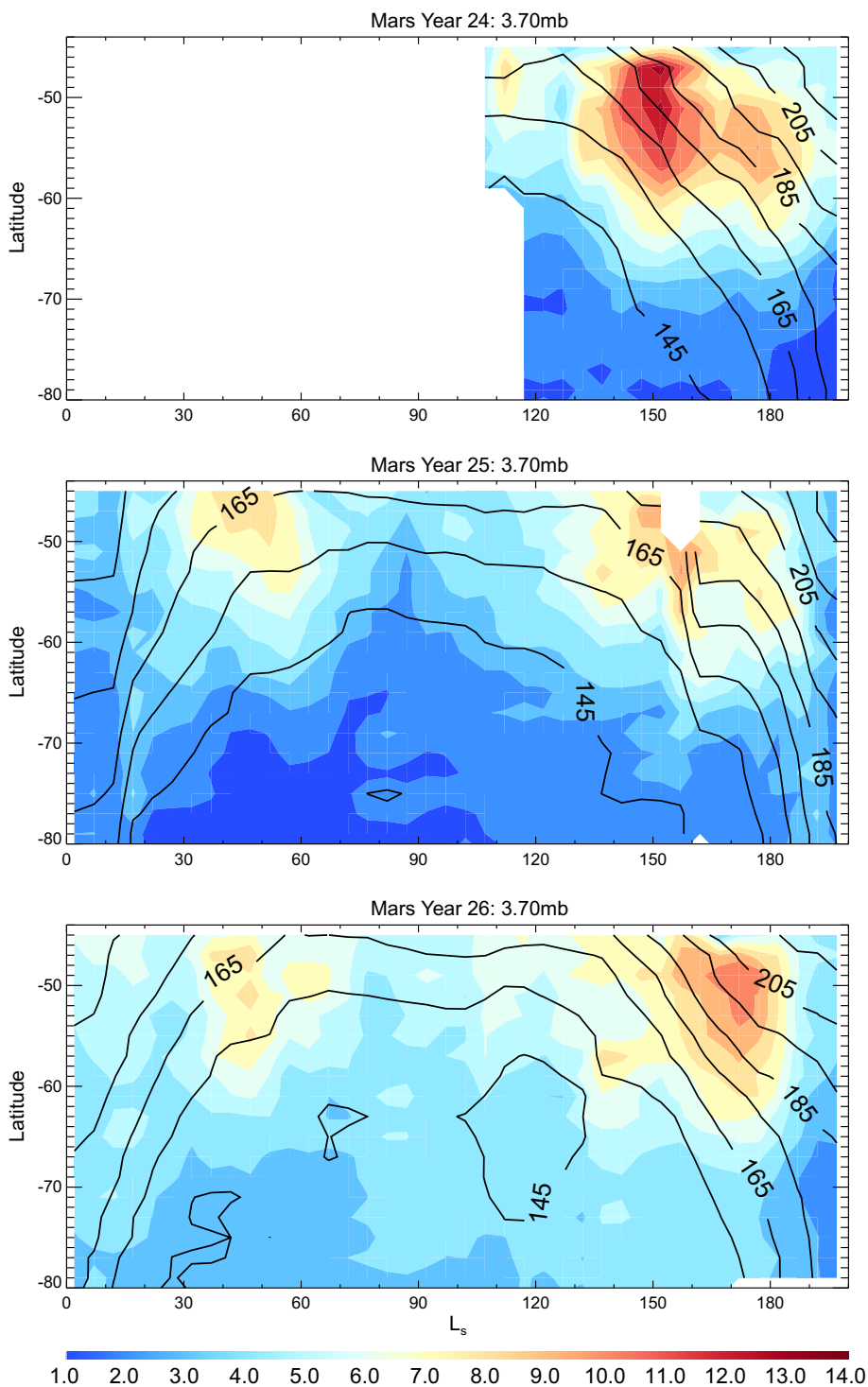
Fig. 4. The filled color contour shows the L_s versus latitude cross section of the standard deviation of TES temperature (K) on the 3.7 mb constant pressure surface at 270°E due to transient eddies whose wave periods are >1 sol and <30 sols. The three panels correspond to Mars Year 24–26. The black contours show the corresponding mean air temperatures at 270°E and 3.7 mb.

in mid southern summer was largely controlled by a mesoscale "sea breeze" circulation between the polar cap and the surrounding terrain. These dust storms did not appear clearly in MDGMs due to their small scales and the overlap area averaging technique used in making the MDGMs (Wang and Ingersoll, 2002). The absence of frontal events in the early summer in Fig. 2 is partly related to the "selection" effect of MDGMs. However, larger events are expected to be less strongly selected against since they tend to be imaged in multiple global map swaths. Therefore, the general pattern depicted for the larger frontal events, which are probably more closely related to the large scale circulation, is more robust.

Southern hemisphere frontal events were also absent in MDGMs during $L_s = 60–140°$, as seen in Fig. 2. During the winter solstice period, the terminator circle is very large which limits the visible imaging observations (Fig. 3). The southern polar hood extended to about 50°S with apparent equatorward extension in Hellas, Argyre and in the region between Thaumasia Fosse and Argyre (50°W and 100°W, Fig. 3). Curvilinear clouds were observed almost daily in the region to the west of the cloud and ice covered Hellas basin (Fig. 3). The cloud is often fibrous and analogous to terrestrial jet streak cirrus. It was not counted as a frontal event in our catalog since it was a daily feature that appeared to be fixed to topography.

Banfield et al. (2004) showed that the transient temperature variation at 3.7 mb was minimal during the southern winter solstice period of Mars Year 25. They used a 30° L_s bin to present the general seasonality of transient eddies. To examine the relationship between frontal events and the temperature variations in more detail, Fig. 4 shows the seasonal and latitudinal distribution of the standard deviation of temperature at 270°E and 3.7 mb for transient eddies whose wave periods were between 1 and 30 sols. The transient temperature perturbations were derived

from the 2 PM TES temperatures by subtracting a linear trend versus time for each 30° longitude × 2° latitude × 15° L_s bin (about 30 sols). The medium number of points in the bins was about 1600. The standard deviation was calculated every 5° of L_s and was returned only if the number of points in the bin was at least 250. The superimposed black contours in Fig. 4 show the average temperature in the bin. The 270°E meridian cuts through the longitudinal sector where frontal events were observed most frequently (Fig. 5a). A similar pattern is obtained when the results for different longitudes are zonally averaged.

Fig. 4 shows that the 1–30 sol period transient eddies were weaker during $L_s = 60–140°$ than during $L_s = 30–60°$ and $L_s = 140–190°$. The absence of frontal events in images during the winter solstice period is consistent with the suppression of lower atmosphere transient eddies shown by these temperature data during the same period. The temperature variation during $L_s = 140–190°$ appears stronger than that during $L_s = 30–60°$ in Fig. 4. This is partly due to the height of the 3.70 mb surface and the vertical distribution of transient temperature variations. The Viking Lander data showed that the surface pressure at $L_s = 50°$ was about 20% larger than that at $L_s = 150°$ (Hess et al., 1977). At 3.75°E and 58.5°S, the topography corrected surface pressure is about 4.9 mb and 4.0 mb at $L_s = 50°$ and $L_s = 150°$, respectively (Smith, 2008). Consequently, the height of the 3.70 mb surface is about 2 km closer to the ground during $L_s = 140–190°$ than during $L_s = 30–60°$. For 3.75°E and 58.5°S at $L_s = 50°$, the transient temperature standard deviation at 4.75 mb is about 10% greater than that at 3.7 mb. Banfield et al. (2004) showed that extra tropical traveling waves usually had an upper level maximum at about 0.3 mb and a lower level maximum at the surface. The 3.70 mb surface intersects the lower level maximum. It is used in Fig. 4 since it is one of the standard pressure levels for TES temperature retrievals. Despite the seasonal
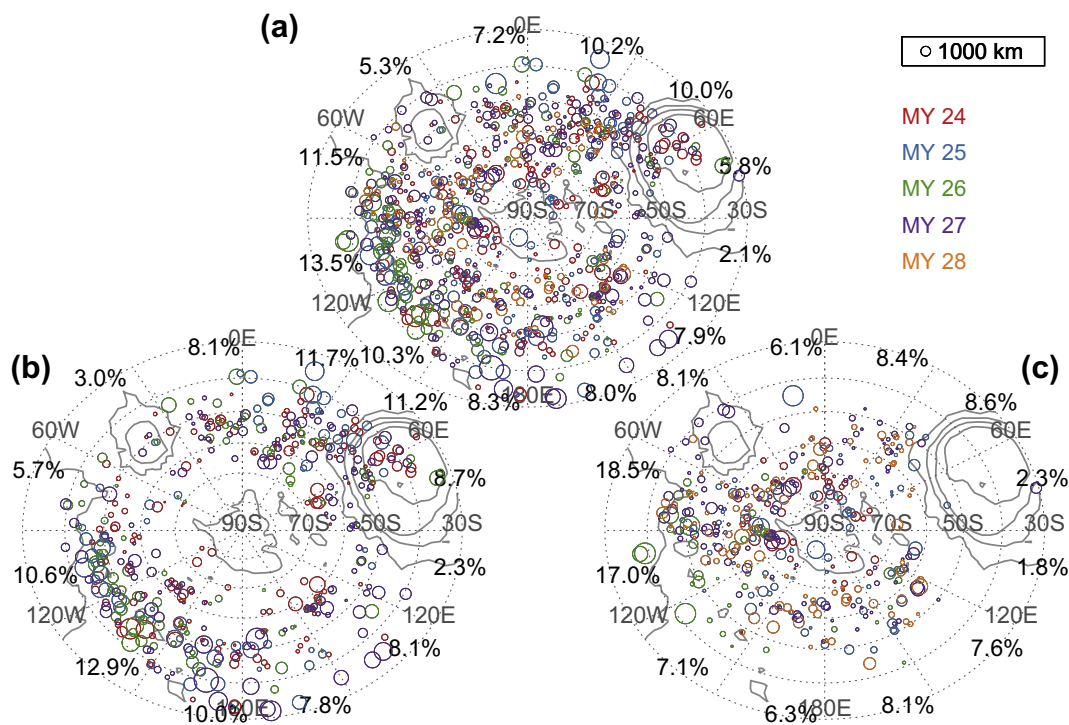
Fig. 5. Longitude–latitude distribution of the southern hemisphere frontal events observed in MGS Mars Daily Global Maps from $L_s = 150°$ in Mars Year 24 to $L_s = 120°$ in Mars Year 28. The polar stereographically projected maps cover the area south of 30°S. The gray contours are the time mean surface pressures from a MarsWRF simulation, for the purpose of indicating major topography. Each circle is centered on the representative point of a frontal event. The diameter of the circle indicates the length of the frontal event (not the latitudinal extent). Different colors are for different Mars years. The percentage of events that occurred within each 30° longitude sector is indicated along the 30°S latitudinal circle. (a) All events during the year, $L_s = 0–360°$ (b) Events from the half year $L_s = 90–270°$ (c) Events from the other half year, $L_s = 270–360–90°$.
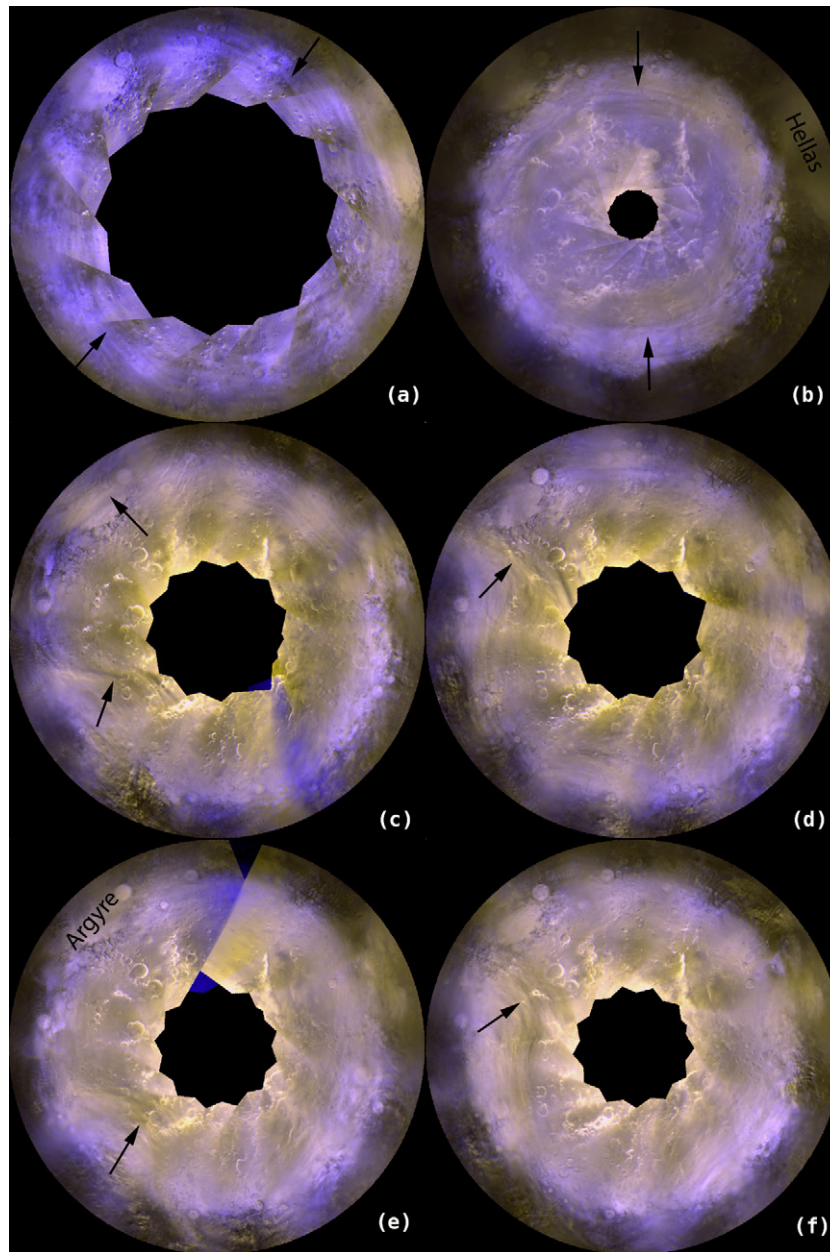
Fig. 6. Streaks in the south polar Mars Daily Global Maps (polar stereographic projection, 45–90°S). (a) $L_s = 139.1°$ in Mars Year 27 (b) $L_s = 179.5°$ in Mars Year 27 (c) $L_s = 158.0°$ in Mars Year 24 (d) $L_s = 158.5°$ in Mars Year 24 (e) $L_s = 164.8°$ in Mars Year 25 (f) $L_s = 165.3°$ in Mars Year 25.

variation of the height of the constant pressure level, the pattern of weak temperature variability during the winter solstice period shown in Fig. 4 is robust.

2.2. Spatial distribution

Fig. 5 shows the spatial distribution of frontal events in the southern hemisphere observed from $L_s = 150°$ in Mars Year 24 to $L_s = 120°$ in Mars Year 28. The percentage of events in each 30° longitude sector is indicated on the plot. The observed events were possibly located slightly downwind of the dust source regions (Wang and Fisher, 2009). Fig. 5a shows events for the full year ($L_s = 0–360°$). The top five most populated sectors, each accounting for more than 10% of the population, are clustered in 60–150°W and 0–60°E. Frontal events were observed less frequently in 60–210°E (East Hellas and its downwind region) and 0–60°W (Argyre and its downwind region). The non-uniform spatial distribution

suggests the presence of storm zones of enhanced transient eddies. Fig. 5b shows results for the winter and spring half of the year ($L_s = 90–270°$). The pattern is similar to that in Fig. 5a, except that the percentage for the 60–90°W sector (upwind of Argyre) decreases substantially and that for the 150–180°W sector increases to 10%. Fig. 5c shows the result for the summer and fall half of the year ($L_s = 270–90°$). The top two most populated sectors account for 18.5% (60–90°W) and 17% (90–120°W) of the population, much greater than those for other sectors.

Using MGS Radio Science data between 67°S and 70°S during $L_s = 134–148°$, Hinson and Wilson (2002) found that there were greater transient temperature variations in the 150–330°E (30–210°W) sector at 3 mb, and that an eastward traveling, nearly 2-sol zonal wave number $m = 3$ wave was dominant at the time. Their simulations using the GFDL Mars GCM reproduced these aspects of the observations. Using TES temperature data, Banfield et al. (2004) presented in their Fig. 19 a prominent storm zone in
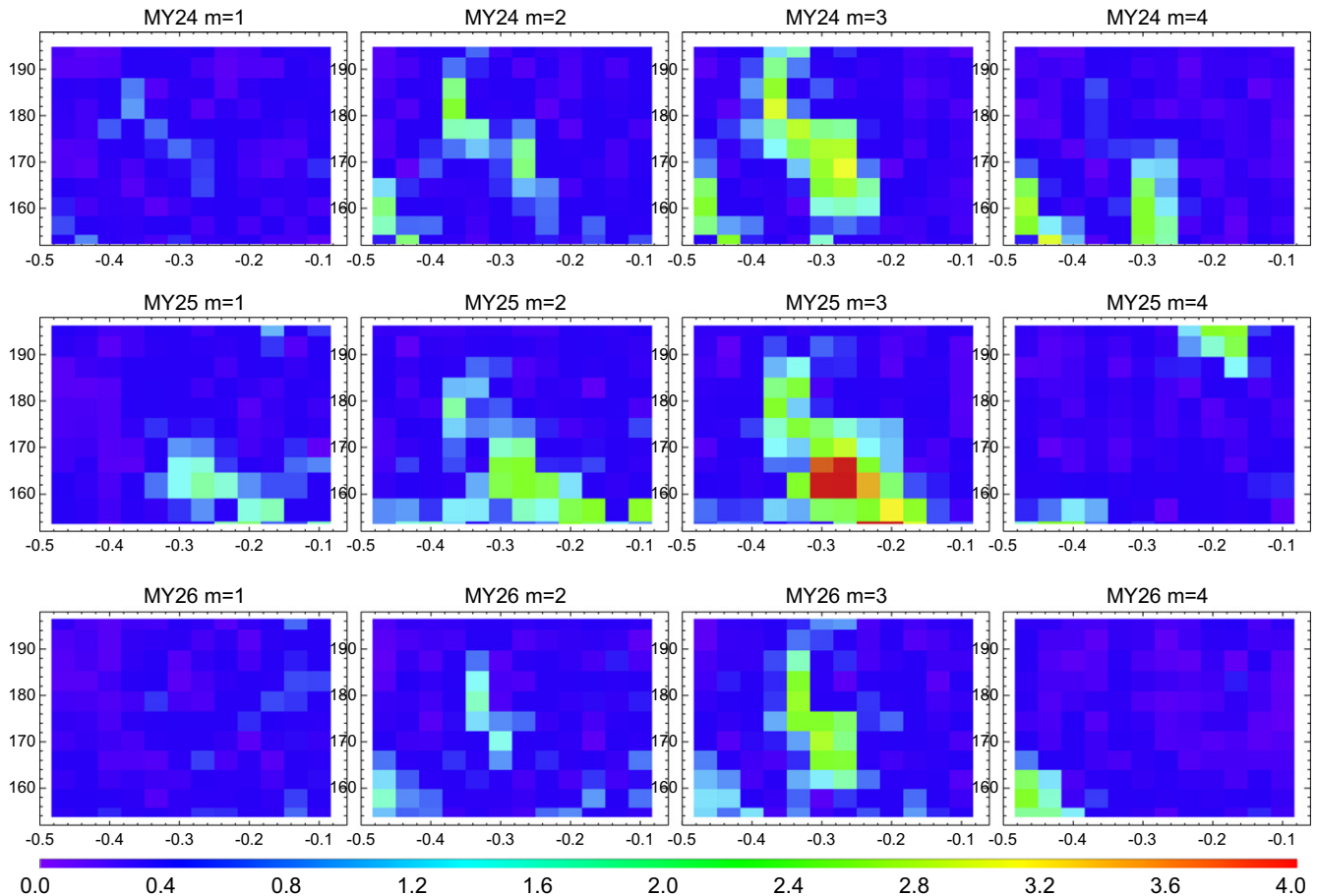
Fig. 7. The amplitudes (K) of eastward traveling waves derived from the 3.7 mb MGS TES temperatures at 51°S as a function of wave frequency (σ, cycle/sol, in the horizontal axis) and L_s (in the vertical axis) for zonal wave numbers $m = 1$–4 and Mars Year (MY) 24–26. Wave period is the inverse of wave frequency. Negative frequency represents an eastward traveling wave.

the 200–300°E (60–160°W) sector and a secondary storm zone in the 30°W–60°E sector at the southern mid and high latitudes at 3.7 mb during $L_s = 15$–75° and $L_s = 105$–195° in Mars Year 24–25. Consistently, our observations using MDGMs show most frequent occurrences of frontal events in the 210–300°E (60–150°W) sector and the 0–60°E sector around the south polar cap (Fig. 5a).

Using the NASA Ames Mars GCM, Colaprete et al. (2005) found that due to the dynamical forcing of Hellas, Argyre and southern Tharsis, the south polar region of Mars was characterized by two distinct regional climates – the cryptic sector (30°E–180°–210°E) was warm and clear and the anti-cryptic sector (150°W–0°–30°E) was cold and stormy. Fig. 5a shows that 42% of the frontal events occurred in the cryptic sector and 58% in the anti-cryptic sector. A Chi square test for the null hypothesis that frontal events occurred with equal frequency in the cryptic and anti-cryptic sector shows that the null hypothesis should be rejected at the 0.1% significance level. Therefore, there were significantly more frontal events in the cold and stormy anti-cryptic sector.

3. Streaks

Kahn (1984) classified elongated features without sharp edges across their long axes as streaks and suggested that streaks were probably related to strong wind or shear. Previous observations suggest that streaks range from local to planetary scales (French et al., 1981; Kahn, 1984; Wang and Ingersoll, 2002). Therefore, the identification of streaks in images depends on the image

resolution and field of view. Viking and Mariner 9 data showed that streaks were widespread over the planet (French et al., 1981; Kahn, 1984). In MGS MDGMs, streaks were prominent in the polar hood (Fig. 6) and often occurred concurrently with other cloud types (Wang and Ingersoll, 2002).

In this paper, we refer to long curvilinear features as "streaks" if they are located over the polar cap and/or they form bundles in the polar hood (Fig. 6). Both frontal events and streaks exhibit curvilinear structure but are in different location. Furthermore, many streaks can be traced in multiple global map swaths that were used to make a MDGM. Collectively, they give an impression of the whole or part of the polar vortex (Fig. 6). We did not archive streaks using MDGMs because of their ubiquity. The color[2] scheme of the MDGMs was designed to emphasize the phenomena away from the polar cap. Our frontal event catalog in Section 2 is for the subset of transient curvilinear features that are outside the polar cap and polar hood. However, reprocessing a subset of MDGMs, we have noticed that in late winter ($L_s = 150$–180°) streaks often deviate from the usual roughly zonal orientation and exhibit wavy structures (Fig. 6c–f). They can either be imagined as segments of the polar vortex or considered as frontal events migrating over the polar cap. Cantor et al. (2010) showed examples of northern springtime frontal storms extending across the seasonal polar cap. We call the curvilinear features over the polar cap in Fig. 6c–f "streaks" in this paper. They were observed most often

---

[2] For interpretation of color in Figs. 1–9, the reader is referred to the web version of this article.
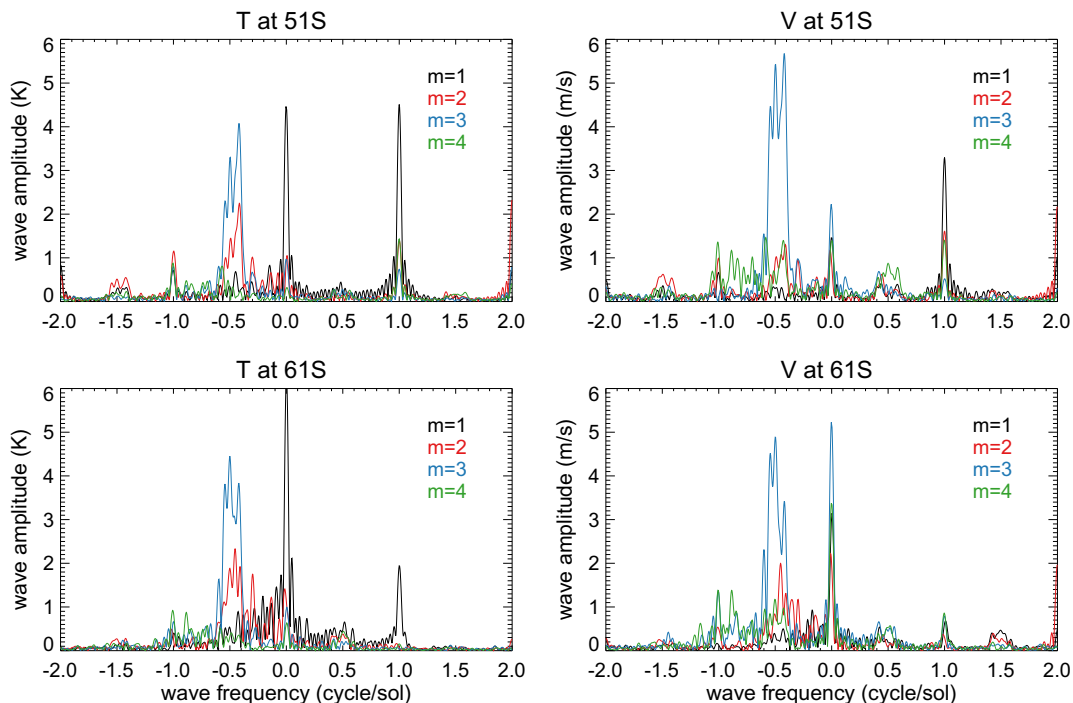
Fig. 8. Wave frequency (σ, cycle/sol, horizontal axis) versus wave amplitude (vertical axis) for the 3.7 mb temperature (*T*, left column, K) and meridional wind (*V*, right column, m/s) at 51°S (top row) and 61°S (bottom row) during L_s = 150–170° derived from a (2° × 2.5° × 40) MarsWRF simulation. Negative wave frequency represents eastward traveling waves, zero frequency represents stationary waves and positive frequency represents westward traveling waves. Zonal waves *m* = 1–4 are in black, red, blue and green, respectively.

in late winter in the longitudinal sector between the 180° meridian and Argyre which is also one of the areas where frontal events preferentially occur (Fig. 5). Had we counted them as frontal events in the catalog, the general seasonal and spatial patterns of frontal events presented in Section 2 would still have remained valid. Regardless of the classification, these long wavy features indicate the presence of planetary waves. The positions and appearances of the streaks varied from day to day (Fig. 6), suggesting the effect of traveling waves.

Fig. 7 shows the amplitudes of the eastward traveling waves with zonal wave number *m* = 1, 2, 3 and 4 in 3.7 mb TES temperatures at 51°S as a function of wave frequency (σ, cycles/sol, negative values indicate eastward phase speed) and L_s during L_s = 150–200° of Mars Year 24–26. Westward traveling waves were usually much weaker than eastward traveling waves (Banfield et al., 2004). Following Wang (2007), traveling waves were derived from TES temperatures using the least squares method of Wu et al. (1995) with a 16-sol sliding window for each 2° latitude × 30° longitude bin. The linear temporal trend within each bin was removed before the wave analysis. Banfield et al. (2004) presented the annual cycle of traveling waves. Here, we focus on the wave spectra in late winter. Fig. 7 shows that there were different mixtures of wave modes for different time periods and that the *m* = 3 waves were dominant most of the time at this latitude. Banfield et al. (2004) pointed out that traveling waves with the same wave period implied storm zones. Fig. 7 shows many such examples. In Mars Year 24, the eastward traveling 2.1 sol (σ = −0.47 cycle/sol) *m* = 2, *m* = 3 and *m* = 4 waves were present during L_s 155–165°, the eastward traveling 3.7 sol *m* = 3 and *m* = 2 waves were present during L_s 165–175° and the eastward traveling 2.7 sol *m* = 3 and *m* = 2 waves were present during L_s 175–190°, etc. In addition to traveling waves, Banfield et al. (2000, 2003) derived strong amplitudes (up to 4 K or more) for zonal wave number *s* = 1 and *s* = 2 stationary waves, and diurnal and semidiurnal tides from TES temperatures in the lower atmosphere of the southern extratropics in

this season. Banfield et al. (2004) pointed out that stationary waves (especially *s* = 1) had a much stronger effect on the zonal winds than traveling waves.

We performed Lagrangian tracer transport experiments to examine the effects of wind components associated with various wave modes on the orientations of streaks and the shape of the polar vortex. Simulations of winds were generated with the MarsWRF Mars GCM (Richardson et al., 2007), with output every 2 h, and were used to drive an off-line Lagrangian tracer transport model. The Lagrangian tracer model uses a fourth order Runge–Kutta method for integration (Eluszkiewicz et al., 1995) and has previously been used to study tracer transport in the Martian atmosphere (Wang et al., 2003). The MarsWRF GCM simulations were conducted with prescribed dust forcing following the "MGS dust scenario" from the Mars Climate Database (Lewis et al., 1999). This spatially and temporally variable dust scenario mimics the dust distribution in Mars Year 24 derived from TES data. The grid-point GCM has 2° latitude × 2.5° longitude horizontal resolution and uses a 40-level vertical structure taken from the GFDL Mars GCM (Wilson and Hamilton, 1996). The model uses the same physics package (including radiative heating associated with CO_2 and dust, diffusive mixing of heat and momentum in the boundary layer, surface and subsurface evolution of temperature, and the treatment of CO_2 condensation and sublimation) as those described by Lee et al. (2009) and the same surface topography, albedo, thermal inertia and terrain slope data as those described by Guo et al. (2009). The model has been shown to compare well with observations of the zonal mean thermal structure, thermal tides, and the seasonal pressure cycle (Guo et al., 2009; Lee et al., 2009; Richardson et al., 2007).

Fig. 8 shows the amplitude versus frequency (σ) for zonal wave number *m* = 1–4 waves derived from the simulated 3.7 mb temperature (*T*) and meridional wind (*V*) at 51°S (top) and 61°S (bottom) during L_s = 150–170°. The analysis was performed on the 2-hourly outputs of the fourth year of a multiannual simulation. The wave
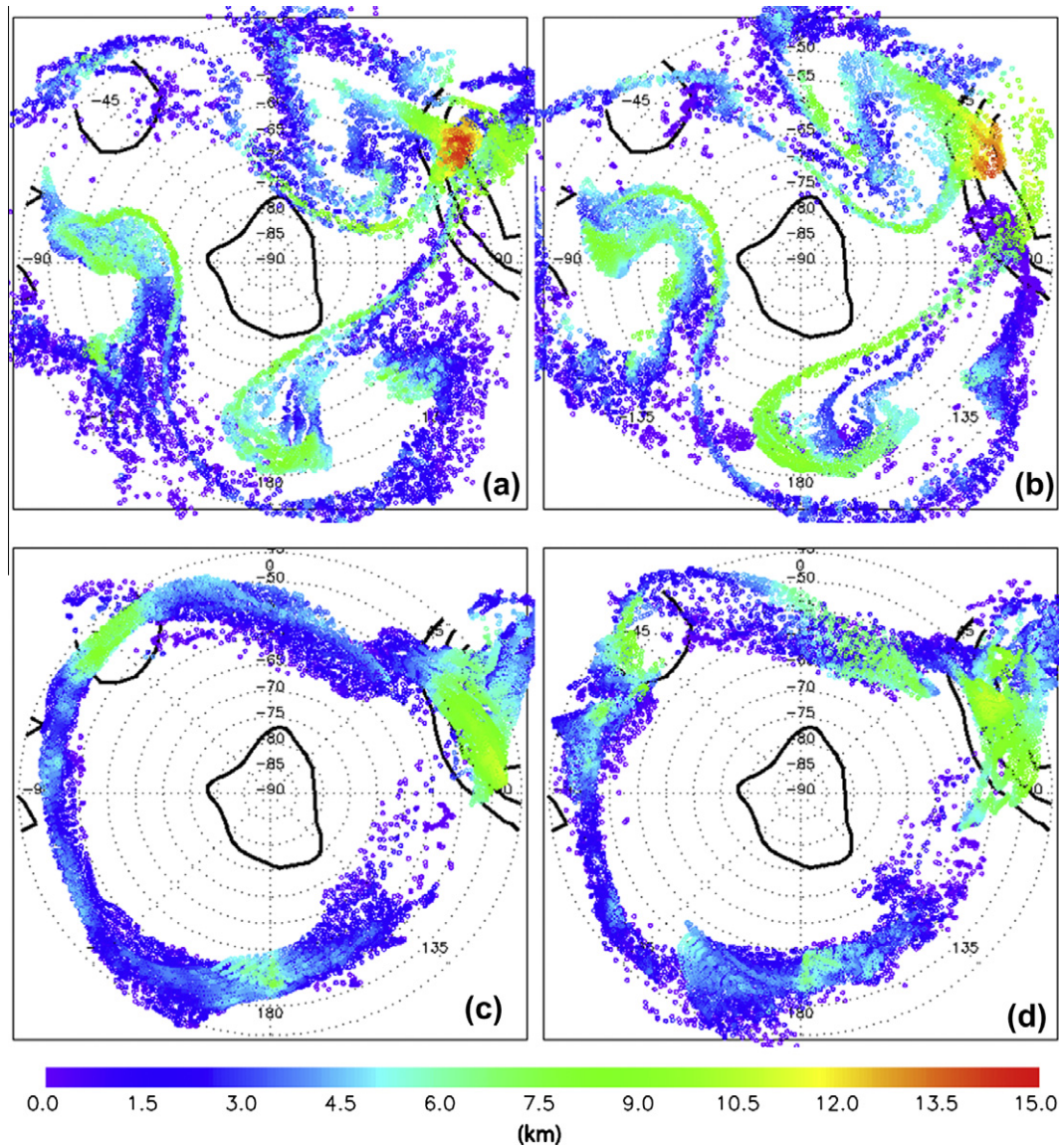
Fig. 9. Snapshots of Lagrangian tracer transport experiments at 26 h after simulation start. The tracers were initialized within the first 15 km of the surface in the latitudinal band between 50°S and 54°S at L$_s$ = 165°. The winds driving the tracer transport model are from a MarsWRF simulation and are subject to the following post processing: (a) none; (b) removal of the stationary waves, diurnal and sub-1 sol components (i.e., retaining only the zonal mean and >1 sol period transients); (c) retaining only the zonal mean and stationary components; (d) including only the zonal mean, stationary, diurnal and sub-1 sol transients. The colors indicate the height of tracer above the local surface. Tracers at low altitudes are plotted before those at high altitudes. The black contours are the simulated mean surface pressure for indicating the topography.

spectra were derived using simple Fourier space–time analysis for L$_s$ = 150–170°. In agreement with the observations presented earlier, the simulated major wave components in temperature output include the westward traveling diurnal (σ = 1.0) and semidiurnal (σ = 2.0) tides, stationary waves (σ = 0), eastward traveling ~2 sol ($\sigma \sim$ −0.5) waves and a hint of eastward traveling diurnal Kelvin waves ($\sigma \sim$ −1.0). The near 2 sol m = 3 waves are the dominant components of the eastward traveling waves, and are accompanied by secondary m = 2 waves of the same frequencies. These waves made major contributions to the simulated storm zones in the lower atmosphere (not shown). The relative importance of different wave components depends on the latitude and also which variable (T or V) is being examined. Fig. 8 shows that the stationary waves were dominated by s = 1 in the temperature field and by s = 3 in the meridional wind field. At 51°S, the ~2 sol eastward traveling m = 3 wave was comparable to the s = 1 stationary wave and the diurnal tide in the temperature field, but was substantially stronger than the other two in the meridional wind field. At 61°S, the ~2 sol

m = 3 eastward traveling wave was about 50% weaker than the s = 1 stationary wave in the temperature field, but was comparable to the s = 3 stationary wave and stronger than the s = 1 stationary wave in the meridional wind field.

We have conducted Lagrangian tracer transport experiments to examine the effects of various wave components in the formation of streaks observed in late winter. Fig. 9 shows the tracer distributions after 26 h of Lagrangian transport. The weightless passive tracers were initialized at L$_s$ = 165° within the first 15 km of the surface in the latitudinal band between 50°S and 54°S (approximately at the edge of the polar cap). The MarsWRF simulated winds were used to drive the tracer transport in Fig. 9a. The tracer distribution exhibits apparent zonal wave number m = 3 structure. Curved bands resembling the wavy streaks in Fig. 6c–f migrate over the polar cap. The whole m = 3 pattern rotates eastward around the south pole at about 120°/sol as each curvilinear band continued to roll up around the corresponding vortex center. At about 48 h, the organized features largely disappear and the

tracers are mixed (not shown), suggesting that the lifetime of these curvilinear features is less than two sols.

Results for sensitivity studies are shown in Fig. 9b–d. In Fig. 9b, the stationary, diurnal and sub-1 sol wind components were filtered out, so that the winds supplied to the Lagrangian tracer transport model included only the modeled zonal mean and the transient eddies (which were dominated by the eastward traveling ~2 sol $m = 3$ wave). The general pattern of tracer distribution is similar to that in Fig. 9a, except that the tracers appear to wrap around the vortex centers slightly more and the whole pattern is more symmetric about the pole. In Fig. 9c, only the time mean winds (including the zonal mean and stationary waves) were used. The majority of tracers are organized into an oval which is offset to the 45°E–0°–135°W hemisphere due mostly to the effect of the $s = 1$ stationary wave. This is consistent with Colaprete et al.'s (2005) result from the NASA Ames Mars GCM that the south polar vortex in winter is located more toward the anti-cryptic sector. The oval of tracers is robust after 96 h. A portion of tracers separates from the oval and moves northward in Hellas and Argyre under the influence of topographically-forced time–mean flow. Fig. 9d shows the effect of the time mean flow, diurnal and sub-1 sol transients. The tracer distribution is similar to Fig. 9c, but appears to have more irregularities along the path. The diurnal and sub-1 sol transients lead to local rotations. But the amplitudes are much smaller than that due to the $m = 3$ traveling wave in Fig. 9b. Overall, Fig. 9 suggests that the ~2 sol $m = 3$ eastward traveling waves are mainly responsible for producing the wavy streaks in Fig. 6c–f and for mixing the air across the south polar vortex edge in late winter. The absence of streaks in other longitudes, which would be necessary to highlight behavior of the whole polar vortex in Fig. 6, is probably due to a lack of dust/condensate.

4. Summary and discussion

In this paper, we report observations and analysis of southern hemisphere curvilinear features (frontal events and streaks) derived from the complete set of MGS Mars Daily Global Maps for the period from $L_s = 150°$ of Mars Year 24 to $L_s = 120°$ of Mars Year 28. We compare the distributions of frontal events in MDGMs with temperature variations derived from TES and other data to examine the relationship between them. Our MDGM observations require the presence of dust or condensate to provide visible features for analysis, and do not include cloud height information. TES temperature observations near the surface have an individual retrieval error of 2 K or more and a vertical resolution of one atmospheric scale height (Conrath et al., 2000). Radio Science (RS) measurements revealed subtle vertical temperature variations at low altitudes not resolvable by TES (Hinson et al., 2004), but the coverage of RS data is sparse.

Frontal events in the southern hemisphere were observed at the edge of the south polar cap within two seasonal periods: $L_s = 340°$–60° and $L_s = 140$–250°. The absence of frontal events in the early and mid summer is consistent with diminished transient eddy activity in the lower atmosphere at these times derived from TES observations (Banfield et al., 2003, 2004). During this period, the polar area is covered by several MOC global map swaths each day. The overlap area is averaged in a MDGM, which tends to smooth out any dust/cloud signatures in a particular image (Wang and Ingersoll, 2002). Therefore, some small (a few hundred kilometers or less) frontal events near the pole may have been left out due to the selection effect. However, larger events are not expected to be as influenced by averaging as they appear in multiple component images. The few small dust plumes observed in MDGMs during this period were not included in our study due to the lack of apparent curvilinear structure. There were two major episodes of

large dust import from tropical latitudes into the south polar region (45–90°S) during mid-summer, and both were related to the regional dust storms initiated by flushing events in Acidalia ($L_s = 316°$ in Mars Year 26 and $L_s = 310°$ in Mars Year 27) (Hinson and Wang, 2010; Wang, 2007). They were not included in this study due to their amorphous morphologies.

Frontal events were rarely recorded in MDGMs during $L_s = 60$–140°. The lack of observable frontal events in images alone does not necessarily mean weaker eddies since it could possibly be related to a lack of dust or condensate. However, TES temperatures show weaker variations in the lower atmosphere during the time period. Therefore, both observations suggest suppressed transient eddies at the polar vortex edge near the surface. Banfield et al. (2004) showed that transient eddies in TES temperatures were characterized by a surface maximum and an upper level maximum, and the seasonal behaviors of the two were different. Specifically, the transient variations aloft were not weaker during this time period. The agreement between the temporal trend of frontal events in MDGMs and that of the near surface temperature variations suggest that our image observations are closely related to lower level atmospheric dynamics.

During the winter solstice period, the terminator circle is very large. As a result, only the outer annulus of the south polar cap and hood is visible in MDGMs in this season. The south polar hood exhibited apparent equatorward extension between Thaumasia Fossae and Argyre during this period (Fig. 3). The only apparent curvilinear feature in this time period was located to the west of Hellas (Fig. 3). We did not include it in our catalog, since it was a daily cloud that appeared to be fixed with respect to the topography. The lack of frontal events and minimized transient eddies at the edge of the polar vortex during the winter solstice period imply the isolation of the polar air from the rest of the atmosphere. Polar air isolation in this season is also suggested by the argon concentrations derived from the Mars Odyssey gamma ray spectrometer data that showed an enrichment of a factor of six of this non-condensable gas over the south polar latitudes near the onset of southern winter (Sprague et al., 2004, 2007).

Frontal events were concentrated in the 210–300°E (60–150°W) sector and the 0–60°E sector around the south polar cap. These regions also exhibited enhanced transient temperature variations in the lower atmosphere (Banfield et al., 2004; Hinson and Wilson, 2002). Using the NASA Ames Mars GCM, Colaprete et al. (2005) found that due mainly to the dynamical forcing by Hellas and Argyre, the south polar vortex was offset to the anti-cryptic region, leading to generally stormier weather in this sector.

Curvilinear features over the polar cap or in the polar hood are called streaks in this paper. In MDGMs, some appear as a bundle of fibers, others as a thick line (sometimes accompanied by fibers). There are no clear distinctions in terms of morphology between a front and a streak. Some streaks form an oval in the polar region, some appear as arcs, and others exhibit wavy segments. A large front at the edge of the polar vortex can potentially transform into a streak by traveling over the polar cap and merging with existing streaks. Wavy streaks were frequently observed between the 180° meridian and Argyre in late winter. A wavy streak (Fig. 6c–f) may be considered as a part of the polar vortex or a frontal event that has migrated over the polar cap. Regardless of the classification, they indicate the influence of planetary waves. TES data and GCM simulations showed prominent stationary waves, diurnal tides and eastward traveling waves during this period. Lagrangian tracer transport experiments suggested that $m = 3$ traveling waves played a key role in making wavy streaks in late winter.

Long term daily global monitoring is critical for studying the martian atmosphere. MGS and MRO have provided great data for detailed studies of martian weather and climate. This paper

summarizes findings from the MGS observations. Similar studies using MRO data will be performed in the future.

Acknowledgments

References

Banfield, D., Conrath, B., Pearl, J.C., Smith, M.D., Christensen, P., 2000. Thermal tides and stationary waves on Mars as revealed by Mars Global Surveyor Thermal Emission Spectrometer. J. Geophys. Res. 105 (E4), 9521–9537.

Banfield, D., Conrath, B.J., Smith, M.D., Christensen, P.R., Wilson, R.J., 2003. Forced waves in the martian atmosphere from MGS TES Nadir data. Icarus 161, 319–345.

Banfield, D., Conrath, B.J., Gierasch, P.J., Wilson, R.J., Smith, M.D., 2004. Traveling waves in the martian atmosphere from MGS TES Nadir data. Icarus 170, 365–403.

Basu, S., Wilson, R.J., Richardson, M.I., Ingersoll, A.P., 2006. Simulation of spontaneous and variable global dust storms with the GFDL Mars GCM. J. Geophys. Res. 111 (E9). doi:10.1029/2005JE002660 (Art. No. E09004).

Benson, J.L., Bonev, B.P., James, P.B., Shan, K.J., Cantor, B.A., Caplinger, M.A., 2003. The seasonal behavior of water ice clouds in the Tharsis and Valles Marineris regions of Mars: Mars Orbiter Camera observations. Icarus 165, 34–52.

Cantor, B.A., 2007. MOC observations of the 2001 Mars planet-encircling dust storm. Icarus 186, 60–96.

Cantor, B.A., James, P.B., Caplinger, M., Wolff, M.J., 2001. Martian dust storms: 1999 Mars Orbiter Camera observations. J. Geophys. Res. – Planets 106, 23653–23687.

Cantor, B.A., James, P.B., Calvin, W.M., 2010. MARCI and MOC observations of the atmosphere and surface cap in the north polar region of Mars. Icarus 208 (1), 61–81. doi:10.1016/j.icarus.2010.01.032.

Clancy, R.T., Sandor, B.J., Wolff, M.J., Christensen, P.R., Smith, M.D., Pearl, J.C., et al., 2000. An intercomparison of ground-based millimeter, MGS TES, and Viking atmospheric temperature measurements: Seasonal and interannual variability of temperatures and dust loading in the global Mars atmosphere. J. Geophys. Res. – Planets 105, 9553–9571.

Colaprete, A., Barnes, J.R., Haberle, R.M., Hollingsworth, J.L., Kieffer, H.H., Titus, T.N., 2005. Albedo of the south pole on Mars determined by topographic forcing of atmosphere dynamics. Nature 435 (7039), 184–188. doi:10.1038/nature03561.

Conrath, B.J., Pearl, J.C., Smith, M.D., Maguire, W.C., Christensen, P.R., Dason, S., et al., 2000. Mars Global Surveyor Thermal Emission Spectrometer (TES) observations: atmospheric temperatures during aerobraking and science phasing. J. Geophys. Res. 105, 9509–9519.

Eluszkiewicz, J., Plumb, R.A., Nakamura, N., 1995. Dynamics of wintertime stratospheric transport in the geophysical fluid-dynamics laboratory SKYHI General Circulation Model. J. Geophys. Res. 100 (D10), 20883–20900.

French, R., Gierasch, P., Popp, B., Yerdon, R., 1981. Global patterns in cloud forms on Mars. Icarus 45, 468–493.

Guo, X., Lawson, W.G., Richardson, M.I., Toigo, A., 2009. Fitting the Viking Lander surface pressure cycle with a Mars General Circulation Model. J. Geophys. Res. – Planets 114. doi:10.1029/2008je003302 (Art. No. E07006).

Hess, S.L., Henry, R.M., Leovy, C.B., Ryan, J.A., Tillman, J.E., 1977. Meteorological results from the surface of Mars: Viking 1 and 2. J. Geophys. Res. 82 (28), 4559–4574.

Hinson, D.P., Wang, H.Q., 2010. Further observations of regional dust storms and baroclinic eddies in the northern hemisphere of Mars. Icarus 206, 290–305. doi:10.1016/j.icarus.2009.08.019.

Hinson, D.P., Wilson, R.J., 2002. Transient eddies in the southern hemisphere of Mars. Geophys. Res. Lett. 29. doi:10.1029/2001gl014103 (Art. No. 1154).

Hinson, D.P., Smith, M.D., Conrath, B.J., 2004. Comparison of atmospheric temperatures obtained through infrared sounding and radio occultation by Mars Global Surveyor. J. Geophys. Res. 109 (E12002). doi:10.1029/2004JE002344.

Kahn, R., 1984. The spatial and seasonal distribution of martian clouds and some meteorological implications. J. Geophys. Res. 89, 6671–6688.

Kahre, M.A., Murphy, J.R., Haberle, R.M., 2006. Modeling the martian dust cycle and surface dust reservoirs with the NASA Ames General Circulation Model. J. Geophys. Res. 111 (E6). doi:10.1029/2005JE002588 (Art. No. E06008).

Lee, C., Lawson, W.G., Richardson, M.I., Heavens, N.G., Kleinbohl, A., Banfield, D., et al., 2009. Thermal tides in the martian middle atmosphere as seen by the Mars Climate Sounder. J. Geophys. Res. – Planets 114. doi:10.1029/2008je003285 (Art. No. E03005).

Lewis, S.R., Collins, M., Read, P.L., Forget, F., Hourdin, F., Fournier, R., et al., 1999. A climate database for Mars. J. Geophys. Res. – Planets 104, 24177–24194.

Rafkin, S.C.R., 2009. A positive radiative–dynamic feedback mechanism for the maintenance and growth of martian dust storms. J. Geophys. Res. 114. doi:10.1029/2008JE003217 (Art. No. E01009).

Richardson, M.I., Toigo, A.D., Newman, C.E., 2007. PlanetWRF: A general purpose, local to global numerical model for planetary atmospheric and climate dynamics. J. Geophys. Res. – Planets 112. doi:10.1029/2006je002825 (Art. No. E09001).

Smith, M.D., 2008. Spacecraft observations of the martian atmosphere. Annu. Rev. Earth Planet. Sci. 36, 191–219. doi:10.1146/annurev.earth.36.031207.124335.

Sprague, A.L., Boynton, W.V., Kerry, K.E., Janes, D.M., Hunten, D.M., Kim, K.J., et al., 2004. Mars' south polar Ar enhancement: A tracer for south polar seasonal meridional mixing. Science 306 (5700), 1364–1367. doi:10.1126/science.1098496.

Sprague, A.L., Boynton, W.V., Kerry, K.E., Janes, D.M., Kelly, N.J., Crombie, M.K., et al., 2007. Mars' atmospheric argon: Tracer for understanding martian atmospheric circulation and dynamics. J. Geophys. Res. 112 (E3). doi:10.1029/2005JE002597 (Art. No. E03S02).

Strausberg, M.J., Wang, H.Q., Richardson, M.I., Ewald, S.P., Toigo, A.D., 2005. Observations of the initiation and evolution of the 2001 Mars global dust storm. J. Geophys. Res. – Planets 110. doi:10.1029/2004JE002361.

Toigo, A.D., Richardson, M.I., Wilson, R.J., Wang, H.Q., Ingersoll, A.P., 2002. A first look at dust lifting and dust storms near the south pole of Mars with a mesoscale model. J. Geophys. Res. 107 (E7). doi:10.1029/2001JE001592 (Art. No. 5050).

Wang, H.Q., 2007. Dust storms originating in the northern hemisphere during the third mapping year of Mars Global Surveyor. Icarus 189, 325–343. doi:10.1016/j.icarus.2007.01.014.

Wang, H.Q., Fisher, J.A., 2009. North polar frontal clouds and dust storms on Mars during spring and summer. Icarus 204, 103–113. doi:10.1016/j.icarus.2009.05.028.

Wang, H.Q., Ingersoll, A.P., 2002. Martian clouds observed by Mars Global Surveyor Mars Orbiter Camera. J. Geophys. Res. – Planets 107. doi:10.1029/2001JE001815.

Wang, H.Q., Ingersoll, A.P., 2003. Cloud-tracked winds for the first Mars Global Surveyor mapping year. J. Geophys. Res. 108 (E9). doi:10.1029/2003JE002107 (Art. No. 5110).

Wang, H.Q., Richardson, M.I., Wilson, R.J., Ingersoll, A.P., Toigo, A.D., Zurek, R.W., 2003. Cyclones, tides, and the origin of a cross-equatorial dust storm on Mars. Geophys. Res. Lett. 30. doi:10.1029/2002GL016828.

Wang, H.Q., Zurek, R.W., Richardson, M.I., 2005. Relationship between frontal dust storms and transient eddy activity in the northern hemisphere of Mars as observed by Mars Global Surveyor. J. Geophys. Res. – Planets 110. doi:10.1029/2005JE002423.

Wilson, R.J., Hamilton, K., 1996. Comprehensive model simulation of the thermal tides in the martian atmosphere. J. Atmos. Sci. 53 (9), 1290–1326.

Wilson, R.J., Neumann, G.A., Smith, M.D., 2007. Diurnal variation and radiative influence of martian water ice clouds. Geophys. Res. Lett. 34 (2). doi:10.1029/2006GL027976 (Art. No. L02710).

Wilson, R.J., Lewis, S.R., Montabone, L., Smith, M.D., 2008. Influence of water ice clouds on martian tropical atmospheric temperatures. Geophys. Res. Lett. 35 (7). doi:10.1029/2007GL032405 (Art. No. L07202).

Wu, D.L., Hays, P.B., Skinner, W.R., 1995. A least-squares method for spectral-analysis of space–time series. J. Atmos. Sci. 52 (20), 3501–3511.